

A Numerical Study of the MHD Metal Oxide Trihybrid Nanofluids ($CuO - MgO - TiO_2/H_2O$) Past a Vertically Radiative Stretching Cylinder in a Porous Medium with Suction, Soret and Dufour Effects

Vaibhav Sanjabarao Bangale^{1*}, Ravindra Kumar¹, and Deepak Kumar¹

¹Department of Mathematics, Vivekananda Global University, Jaipur (Raj.), India

Abstract: The present work looks into how heat and concentration layering influence the MHD flow of a ternary hybrid nanofluid over a radiative, stretching vertical cylinder placed in a porous medium. The working fluid is a mixture of water with CuO , MgO , and TiO_2 nanoparticles, chosen for their ability to improve thermal and mass-transfer performance. After applying similarity transformations, the boundary-layer equations are converted into ordinary differential form and solved using MATLAB's `bvp4c` routine. From the numerical data, several patterns are evident. A higher magnetic field, higher porous resistance, higher Prandtl number, and the presence of Soret, Dufour, suction, and thermal stratification tend to slow down the flow. Conversely, an increase in the curvature of the cylinder, heat generation, radiation, viscous heating, and buoyancy help to accelerate the flow. In general, the temperature declines as curvature, buoyancy, radiation, heat generation, viscous dissipation, stratification, Lewis number, or concentration of nanoparticles increase. In contrast, the temperature tends to increase when magnetic field strength, permeability, and the Prandtl number are strengthened. Concentration decreases with buoyancy, curvature, Lewis number, Dufour effect, or solutal stratification but increases with a magnetic field, permeability, Prandtl number, or thermal stratification. These trends provide insight into the hybrid nanofluid behavior in porous cylindrical systems.

1. Introduction

The ternary mixture of copper oxide (CuO), Magnesium oxide (MgO), and Titanium dioxide (TiO_2) dispersed in water is considered an ideal hybrid nanofluid for improving thermal and mass-transfer performance due to the synergistic combination of high thermal conductivity, structural stability, and superior flow behavior. Heat and mass transfer analysis with moving cylinders receive particular focus in numerous manufacturing processes for reliable equipment design. Tangent hyperbolic nanofluid flow impinging on moving cylinders is an extensive area of study. Numerous investigation viewpoints have been broadened by its wide range of manufacturing and engineering applications, such as the extraction of plastic and rubber sheets, cooling and drying of papers and textiles, glass blowing, glass fiber, hot rolling polymer processing industries, textile production, wire drawing, petroleum production, crystal growing, cooling of nuclear reactors, and fiber spinning. The Soret and Dufour effects play an important role in fluid flow through porous media by coupling heat and

mass transfer in oil and gas reservoirs. Understanding these effects aids in enhanced oil recovery, hydrocarbon migration modeling, and prediction of long-term compositional changes. Xie et al. [1] Ethylene glycol was utilized as the fundamental fluid and five various oxide types—magnesium oxide (MgO), TiO_2 , ZnO , Al_2O_3 , and SiO_2 nanoparticles—were chosen as additives and generate stable nanofluids. Suresh et al. [2] examined a powder mixture of Al_2O_3 and Cu in 90:10 weight proportions generated using a chemical route synthesis was used to create Al_2O_3 - Cu hybrid particles using the hydrogen reduction approach. Mohamed et al., [3] presented a mathematical description of the mixed convection boundary layer flow within a horizontal circular cylinder in a nanofluid with the presence of the viscous dissipation effect. Chamkha et al. [4] The MHD flow and heat transmission of a hybrid nanofluid between two surfaces in a rotating system is investigated. Maskeen et al. [5] The flow characteristics and heat transfer performance of an alumina-copper/water (Al_2O_3 - Cu/H_2O) hybrid

*Corresponding author: vaibhavbangale456@gmail.com

nanofluid over a stretching cylinder under the influence of thermal radiation and Lorentz magnetic forces are explored in the study. Ali et al. [6] discussed the thermo-diffusion and diffusion-thermo phenomena in a semi-infinite absorbent channel with expanding and contracting walls and heat source/sink effects. Aminian et al. [7] examined the Studied of quantitatively MHD forced convection effects of Al_2O_3 -Cu-water nanofluid inside a partitioned cylinder within a porous material. El-Zahar et al. [8] investigated to analysis the magneto-mixed convective flow of an aqueous-based hybrid nanofluid including copper and alumina nanoparticles over a horizontal circular cylinder with a convective boundary condition. Filahi et al. [9] investigated the consequences of thermo-diffusion and diffusion-thermo on double-diffusive natural convection created in a horizontal Brinkman porous layer with a stress-free top boundary. Khashi et al. [10] aimed to (i) notice the duality of solutions; and (ii) investigate the flow and heat transfer of the hybrid nanofluid in a shrinking cylinder as Joule heating is present. A single-phase nanofluid model with changed thermophysical parameters is the mathematical model. Kristiawan et al. [11] A hybrid approach using a microfin tube and TiO_2 /water nanofluid with various nanoparticle concentrations has been investigated effectively Kumar et al. [12] The MHD pulsatile flow of Casson nanofluid along a vertical channel embedded in a porous medium with thermal radiation and heat generation/absorption was studied in this research with the Buongiorno model. Joule's dissipations and viscosity are examined. Ma et al. [13] The synergistic mechanism of improved thermal conductivity and associated economic analysis are examined so as to choose a suitable nanofluid. The effects of base fluid (BF) mixing ratios and nanoparticles (NP) on thermal conductivity enhancement (Al_2O_3 - Cu - TiO_2 / EG-W, Al_2O_3 -CuO / EG-W, and Al_2O_3 - Cu /EG-W) are investigated at 1.0 vol% and temperatures between 20 °C and 60 °C. Okello et al. [14] examined three types of ethylene glycol-based hybrid nanofluids (Al_2O_3 - Cu), (Cu - TiO_2), and (TiO_2 - Al_2O_3) to determine their cooling capacities for industrial cooling applications. Roy et al. [15] The effects of thermal radiation and viscous dissipation on the flow and heat transfer of a hybrid nanofluid (Al_2O_3 - Cu /water) in a circular cylinder are examined for both opposing and aiding flows. Shafie et al. [16] examined the effect of viscous dissipation on steady two-dimensional mixed convection flow in a horizontal circular cylinder in a viscoelastic

nanofluid with convective boundary conditions. Zhou et al. [17] studied a numerical model of double diffusive natural convection under the Soret and Dufour effect is shown. The concentration, temperature, and flow field distributions, as well as the variation of the average Sherwood and Nusselt numbers, are examined relative to various Rayleigh numbers (ranging from 103 to 107), Lewis numbers (ranging from 0.5 to 8), buoyancy ratios (ranging from -5 to 5), and Soret and Dufour (ranging from 0 to 0.5). Meena et al. [18] The effect of Soret and Dufour effects on mixed convection flow across a vertical cone with injection/suction effects is researched throughout the study. Qureshi et al., [19] studied the mass and heat energy transport method under temperature and concentration gradients. Reddy et al. [20] The Darcy-Forchheimer Prandtl fluid flow formed by a moving sheet is covered in this article. The widely accepted energy transfer model, the Cattaneo-Christov model of heat transfer, is used under thermal radiation. Venkateswarlu and Satyanarayana [21] Hybrid nanofluids are complex fluid classes with enhanced thermal properties that operate better than traditional nanofluids, due of recent developments in nanotechnology research. Yesodha et al. [22] studied the characteristics of heat flow, mass transfer, and activation energy related to a chemically reacting viscous fluid in a rotating frame. The impact of the Soret and Dufour factors is investigated as well. Hanafi et al., [23] studied the heat transfer efficiency of several nanofluid coolants via a single nozzle, axisymmetric, limitations impingement jet approach. Raza et al., [24] analysed the thermal features of nanofluid with kerosene oil and water base fluid with inclined magnetic force. The sloping surface induced the flow. Asghar et al., [25] A mathematical investigation has been undertaken on the convective Jeffery-Hamel flow problem in the presence of diffusion-thermo and thermo-diffusion effects. Chepak-Gizbrekht and Knyazeva [26] article given a mathematical model of the process of heat treatment the surface of a solid material using a brief thermal impulse, as correspond to a laser generated on the line. Huang [27] examined the heat and mass that are exchanged when a fluid experiences convective flow along an inclined plate via a porous surface, as well as the associated chemical reaction and activation energy. Imran et al. [28] investigated the effect of Soret and Dufour on the flow of a time-dependent couple stress fluid across a flexible curved oscillatory surface with a magnetic field. The oscillation of the surface is what induces the flow phenomenon. Li et al. [29]

examined the study of chemically reactive Darcy-Forchheimer nanoliquid flow toward a stretched surface. Buongiorno's model is used for the importance of nanoliquids. Additionally, Soret and Dufour characteristics are taken into account. Mishra et al. [30] examined the effect of Soret and Dufour on MHD nanofluid flow via a composite stenosed artery with temperature-dependent viscosity. Patil et al., [31] examined the flow of tangent hyperbolic (TH) ternary hybrid nanofluid (THNF) over a rough-yawed cylinder caused by impulsive motion in a mixed convection mechanism with periodic magnetohydrodynamics Rehman et al. [32] examined Heat transfer and hydromagnetic flow are sustainable elements of traditional system design, along with geothermal energy structures and high-performance thermal equipment. Shafiq et al., [33] studied the application of nanotechnology has made possible many current and more efficient applications, this includes the generation of solar power, the reconstruction of heat exchange systems, and the modernization of the pharmaceutical and medical industries. Yasir et al. [34] The thermal performance of hybrid nanofluids has become an issue of an increasing number of research investigations in the literature. In order to determine the thermophysical characteristics of nanofluids, theoretical correlations have been extensively investigated. Farooq et al. [35] studied the potential of MHD bioconvective micropolar nanofluids by a non-similarity analysis without taking into account the effect of Soret and Dufour effects. Identifying the complex mass and heat transfer phenomena inherent in both biological and industrial systems is the goal. Nath and Deka [36] The primary objective of this research is to find out if thermal stratification affects the magnetohydrodynamics MHD flow of water-based nano, hybrid, and ternary hybrid nanofluids as they flow by a vertically expanding cylinder of a porous medium. Naz et al., [37] examined the flow of ternary hybrid nanomaterials in pore spaces in the presence of magnetohydrodynamics (MHD) and nonlinear convection. Three distinct nanoparticles are used: alumina (Al_2O_3), copper (Cu), and magnesium oxide (MgO). Sudarmozhi et al. [38] studied how non-Newtonian fluids operate in natural settings, like rivers and groundwater flow, in order to evaluate the effect on the environment. The Soret and Dufour effects have significant effects on the movement of pollutants and heat in these systems. Ullah et al. [39] examined the thermal radiation and Soret/Dufour significantly rise mass and heat transmission in material science, geothermal processes, chemical

rectors, and heat exchangers due to temperature and variations in nanoparticle concentration. Venkateswarlu et al. [40] examined the impact of suction/injection on the thermally radiated convective flow generated by a nonlinear stretched disk.

1.2 Mathematical Formulation

A two-dimensional, steady, incompressible ternary hybrid nanofluid composed of $CuO - MgO - TiO_2$ nanoparticles dispersed in water is examined as it moves through a porous medium surrounding a vertically oriented, stretchable cylinder of radius r_0 . The flow is influenced by thermal stratification in the ambient environment as well as an internal heat source or sink. As illustrated in Figure 1, the nanofluid travels in the axial x -direction along the surface of the cylinder, while the radial coordinate r denotes the direction perpendicular to the axis of motion.

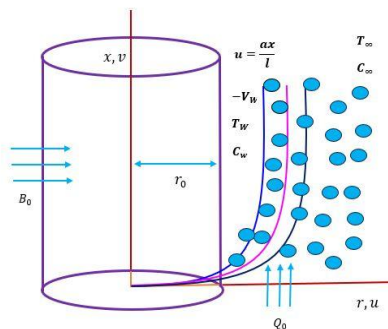


Fig. 1. Flow geometry of the ternary hybrid nanofluid over a vertical stretching cylinder.

In this context, the variables u and v represent the velocity components of the ternary hybrid nanofluid along the r and x - axes, respectively. In this study, a magnetic field with a magnitude of B_0 is applied in a direction perpendicular to the propagation of the ternary hybrid nanofluid. The flow issue takes into account the thermal buoyancy effect while disregarding the Joule's impact. The velocity that causes linear stretching of the vertical cylinder is denoted as $U = \frac{ax}{l}$ where a and l represent the velocity and characteristic length of the cylinder, respectively. $T_\infty(x) = T_0 + A \left(\frac{x}{l}\right)$, and $C_\infty(x) = C_0 + C \left(\frac{x}{l}\right)$, represents the assumed temperature and concentration of the wall, while $T_\infty(x) = T_0 + B \left(\frac{x}{l}\right)$ and $C_\infty(x) = C_0 + D \left(\frac{x}{l}\right)$ represents the temperature and

concentration of the ternary hybrid nanofluid at the ambient condition, where A, B, C, D and T_0, C_0 are non-negative constants and the starting temperature and

$$\frac{\partial(ru)}{\partial x} + \frac{\partial(rv)}{\partial r} = 0, \tag{1}$$

$$u \frac{\partial u}{\partial x} + v \frac{\partial u}{\partial r} = \frac{\mu_{thnf}}{\rho_{thnf}} \frac{1}{r} \frac{\partial}{\partial r} \left(r \frac{\partial u}{\partial r} \right) - \frac{\sigma_{thnf}}{\rho_{thnf}} B_0^2 u - \frac{\mu_{thnf}}{\rho_{thnf}} \frac{u}{K^*} + \frac{(\rho\beta)_{thnf}}{\rho_{thnf}} g(T - T_\infty), \tag{2}$$

$$u \frac{\partial T}{\partial x} + v \frac{\partial T}{\partial r} = \frac{k_{thnf}}{(\rho C_p)_{thnf}} \frac{1}{r} \frac{\partial}{\partial r} \left(r \frac{\partial T}{\partial r} \right) + \frac{Q_0}{(\rho C_p)_{thnf}} (T - T_\infty) - \frac{1}{(\rho C_p)_{thnf}} \frac{1}{r} \frac{\partial}{\partial r} (r q_r) + \frac{\sigma_{thnf}}{(\rho C_p)_{thnf}} B_0^2 u^2 + \frac{\mu_{thnf}}{(\rho C_p)_{thnf}} \left(\frac{\partial u}{\partial r} \right)^2 + \frac{D_{thnf} K_T}{C_p C_s} \frac{1}{r} \frac{\partial}{\partial r} \left(r \frac{\partial C}{\partial r} \right), \tag{3}$$

$$u \frac{\partial C}{\partial x} + v \frac{\partial C}{\partial r} = D_{thnf} \frac{1}{r} \frac{\partial}{\partial r} \left(r \frac{\partial C}{\partial r} \right) + \frac{D_{thnf} K_T}{T_m} \frac{1}{r} \frac{\partial}{\partial r} \left(r \frac{\partial T}{\partial r} \right), \tag{4}$$

The boundary conditions governing the system can be expressed as:

$$u = \frac{ax}{l}, v = -v_w(x), T = T_w(x), C = C_w(x) \tag{5}$$

when $r = r_0$

$$u = 0, T \rightarrow T_\infty(x), C \rightarrow C_\infty(x) \tag{6}$$

as $r \rightarrow \infty$,

The similarity transformation used as

$$\eta = \frac{r^2 - r_0^2}{2r_0} \sqrt{\frac{a}{v_f l}}, \quad \psi = \sqrt{\frac{av_f}{l}} x r_0 f(\eta), \quad \theta = \frac{T - T_\infty(x)}{T_w(x) - T_0},$$

$$\phi = \frac{C - C_\infty(x)}{C_w(x) - C_0},$$

The stream function ψ is introduced to satisfy continuity equation Eq. (1) in the manner that

$$u = \frac{1}{r} \frac{\partial \psi}{\partial r} \text{ and } v = -\frac{1}{r} \frac{\partial \psi}{\partial x}.$$

Hence, the non-dimensional forms of the transformed equations are given by

$$a2(f'^2 - 2ff'') = a1(2\gamma f'' + (1 + 2\gamma\eta)f''') - (a3M + a1K)f' + a4\lambda\theta, \tag{7}$$

$$a6\{(\theta + \delta_1)f' - f\theta'\} = (a5 + Ra)(pr)^{-1}(2\gamma\theta' + (1 + 2\gamma\eta)\theta'') + Q\theta + a1Ec(1 + 2\gamma\eta)f''^2 + a3MEcf'^2 + a6Du(2\gamma\phi' + (1 + 2\gamma\eta)\phi''), \tag{8}$$

$$(\phi + \delta_2)f' - f\phi' = a7(Le)^{-1}(2\gamma\phi' + (1 + 2\gamma\eta)\phi'') + a7Sr(2\gamma\phi' + (1 + 2\gamma\eta)\phi''), \tag{9}$$

Here

$$a1 = \frac{\mu_{thnf}}{\mu_f}, a2 = \frac{\rho_{thnf}}{\rho_f}, a3 = \frac{\sigma_{thnf}}{\sigma_f}, a4 = \frac{(\rho\beta)_{thnf}}{(\rho\beta)_f}, a5 = \frac{k_{thnf}}{k_f}, a6 = \frac{(\rho C_p)_{thnf}}{(\rho C_p)_f}, a7 = \frac{D_{thnf}}{D_f},$$

$\mu_{thnf}, \rho_{thnf}, \sigma_{thnf}, \beta_{thnf}, k_{thnf}, (C_p)_{thnf}, D_{thnf}$, the symbols represent the ternary hybrid nanofluids coefficient of viscosity, density, electrical conductivity, thermal expansions coefficient, thermal conductivity, heat capacity and mass diffusivity, respectively. Also, $\mu_f, \rho_f, \sigma_f, \beta_f, k_f, (C_p)_f, D_f$, denote the base fluids coefficient of viscosity, density, electrical conductivity, thermal expansions coefficient, thermal conductivity, heat capacity and mass diffusivity correspondingly. $\gamma =$

concentration, correspondingly. The governing equations for continuity, momentum, and energy in the context of a ternary mixture tiny liquid can be expressed as follows

$\sqrt{\frac{lv_f}{ar_0^2}}$ is the curvature parameter, $M = \frac{B_0^2 l \sigma_f}{a \rho_f}$ is the magnetic parameter, $K = \frac{lv_f}{aK^*}$ is the permeability parameter, $\lambda = \frac{Gr_x}{Re_x^2}$ is the thermal buoyancy parameter where $Gr_x = g\beta_r(T_w - T_\infty) \frac{x^3}{\nu^2}$ is local Grashof number, and $Re_x = \frac{xU_w}{\nu_f}$ is local Reynolds number, $Pr = \frac{(\rho C_p)_f \nu_f}{k_f}$ denotes Prandtl number, $Ra = \frac{16\sigma^* T_\infty^3}{3k_f k^*}$ is radiation parameter, $Q = \frac{Q_0 l}{a(\rho C_p)_f}$ heat source/sink parameter, $Ec = \frac{U^2}{(C_p)_f (T_w(x) - T_\infty(x))}$ is the Eckert number,

$Le = \frac{D_f}{\nu_f}$ denotes Lewis number, $Du = \frac{D_f K_T [C_w(x) - C_\infty(x)]}{C_p C_s [T_w(x) - T_\infty(x)]}$ represents Dufour number, $Sr = \frac{D_f K_T [T_w(x) - T_\infty(x)]}{T_m [C_w(x) - C_\infty(x)]}$ represents Soret number. The transformed boundary conditions are as follows and we provide non-dimensional quantities as the followings.

$$f(0) = S, f'(0) = 1, \theta(0) = 1 - S_1, \phi(0) = 1 - \delta_2, \tag{10}$$

when $\eta \rightarrow 0$

$$f'(\infty) \rightarrow 0, \theta(\infty) \rightarrow 0, \phi(\infty) \rightarrow 0, \tag{11}$$

as $\eta \rightarrow \infty$

Here $S = \sqrt{\frac{l}{av_f}} v_w$, is the suction parameter, $\delta_1 = \frac{B}{A}$ is the thermal stratification parameter, and $\delta_2 = \frac{D}{C}$ is the concentration stratification parameter.

The physical quantities, skin friction coefficient, the local Nusselt number and local Sherwood number are defined as follows

$$C_{fx} = \frac{\tau_w}{\rho U_w^2}, \tag{12}$$

$$Nu_x = \frac{xq_w}{k_f(T_w - T_\infty)}, \tag{13}$$

$$Sh_x = \frac{xq_m}{D_b(C_w - C_\infty)} \tag{14}$$

Here $\tau_w = \mu_{thnf} \left(\frac{\partial u}{\partial r} \right)_{r=r_0}$, $q_w = -k_{thnf} \left(\frac{\partial T}{\partial r} \right)_{r=r_0} + (q_r)_{r=r_0}$, $q_m = - \left(D_{thnf} \frac{\partial C}{\partial y} \right)_{r=r_0}$,

$$C_{fx} (Re_x)^{\frac{1}{2}} = a1f''(0), \tag{15}$$

$$Nu_x (Re_x)^{-\frac{1}{2}} = - \left(\frac{a5+Ra}{1-\delta_1} \right) \theta'(0), \tag{16}$$

$$Sh_x (Re_x)^{-\frac{1}{2}} = - \frac{a7}{1-\delta_2} \phi'(0), \tag{17}$$

Table 1: The thermo-physical characteristics of trihybrid nanofluid are as follows

Viscosity

$$a1 = \frac{\mu_{thnf}}{\mu_f} = \frac{1}{(1 - \phi_1)^{2.5}(1 - \phi_2)^{2.5}(1 - \phi_3)^{2.5}},$$

Density

$$a2 = \frac{(\rho)_{thnf}}{(\rho)_f} = (1 - \phi_3) \left[(1 - \phi_2) \left\{ 1 - \phi_1 + \phi_1 \frac{(\rho)_{nf1}}{(\rho)_f} \right\} + \phi_2 \frac{(\rho)_{nf2}}{(\rho)_f} \right] + \phi_3 \frac{(\rho)_{nf3}}{(\rho)_f},$$

Electrical conductivity

$$\frac{\sigma_{nf}}{\sigma_f} = \frac{[(\sigma_{nf1} + 2\sigma_f) - 2\phi_1(\sigma_f - \sigma_{nf1})]}{[(\sigma_{nf1} + 2\sigma_f) + 2\phi_1(\sigma_f - \sigma_{nf1})]} \cdot \frac{\sigma_{hnf}}{\sigma_f} = \frac{[(\sigma_{nf2} + 2\sigma_{nf}) - 2\phi_2(\sigma_{nf} - \sigma_{nf2})]}{[(\sigma_{nf2} + 2\sigma_{nf}) + 2\phi_2(\sigma_{nf} - \sigma_{nf2})]}$$

$$\frac{\sigma_{thnf}}{\sigma_{hnf}} = \frac{[(\sigma_{nf3} + 2\sigma_{hnf}) - 2\phi_3(\sigma_{hnf} - \sigma_{nf3})]}{[(\sigma_{nf3} + 2\sigma_{hnf}) + 2\phi_3(\sigma_{hnf} - \sigma_{nf3})]}, a3 = \frac{\sigma_{thnf}}{\sigma_f}$$

thermal expansion coefficient

$$a4 = \frac{(\rho\beta_T)_{thnf}}{(\rho\beta_T)_f} = (1 - \phi_3) \left[(1 - \phi_2) \left(1 - \phi_1 + \phi_1 \frac{(\rho\beta_T)_{nf1}}{(\rho\beta_T)_f} \right) + \phi_2 \frac{(\rho\beta_T)_{nf2}}{(\rho\beta_T)_f} \right] + \phi_3 \frac{(\rho\beta_T)_{nf3}}{(\rho\beta_T)_f},$$

Thermal conductivity

$$\frac{k_{nf}}{k_f} = \frac{[(k_{nf1} + 2k_f) - 2\phi_1(k_f - k_{nf1})]}{[(k_{nf1} + 2k_f) + 2\phi_1(k_f - k_{nf1})]} \cdot \frac{k_{hnf}}{k_{nf}} = \frac{[(k_{nf2} + 2k_{nf}) - 2\phi_2(k_{nf} - k_{nf2})]}{[(k_{nf2} + 2k_{nf}) + 2\phi_2(k_{nf} - k_{nf2})]}$$

$$\frac{k_{thnf}}{k_{hnf}} = \frac{[(k_{nf3} + 2k_{hnf}) - 2\phi_3(k_{hnf} - k_{nf3})]}{[(k_{nf3} + 2k_{hnf}) + 2\phi_3(k_{hnf} - k_{nf3})]}, a5 = \frac{k_{thnf}}{k_f},$$

Heat Capacity

$$a6 = \frac{(\rho C_p)_{thnf}}{(\rho C_p)_f} = (1 - \phi_3) \left[(1 - \phi_2) \left\{ 1 - \phi_1 + \phi_1 \frac{(\rho C_p)_{nf1}}{(\rho C_p)_f} \right\} + \phi_2 \frac{(\rho C_p)_{nf2}}{(\rho C_p)_f} \right] + \phi_3 \frac{(\rho C_p)_{nf3}}{(\rho C_p)_f},$$

Mass diffusivity

$$a7 = \frac{D_{thnf}}{D_f} = ((1 - \phi_1)(1 - \phi_2)(1 - \phi_3))^{-1},$$

where ϕ_1, ϕ_2, ϕ_3 are volume fraction of Cu, Al_2O_3 and TiO_2 tiny particles respectively. The suffixes $thnf, hnf, nf, f, nf_1, nf_2, nf_3$, denote ternary mixture tiny liquid, mixture tiny liquid, tiny liquid, base liquid, solid tiny particles of Cu, Al_2O_3 and TiO_2 correspondingly.

Table 1: Thermo-physical properties of Cu, MGO and TiO_2 tiny particles in pure water are presented.

Physical Properties	H ₂ O (base fluid)	Cu(nf ₁)
$\rho(Kg/m^3)$	997.1	6510
$C_p(J/KgK)$	4179	540
$k(W/mK)$	0.613	18
$\beta \times 10^5(K^{-1})$	21	0.85
$\sigma(s/m)$	5.5×10^{-6}	5.96×10^7
Physical Properties	$MgO (nf_2)$	$TiO_2 (nf_3)$
$\rho(Kg/m^3)$	3560	4250
$C_p(J/KgK)$	955	686.2
$k(W/mK)$	45	8.9538
$\beta \times 10^5(K^{-1})$	1.05	0.9
$\sigma(s/m)$	8×10^{-6}	2.38×10^6

Method of Solution:The outcome produced by equations (7), (8), and (9) collectively under borderline conditions (10) and (11) is established using a systematic numerical approach known as the shooting technique. This involves transforming the nonlinear equations into first-order ordinary differential equations by assigning variables, namely

$$f = f_1, f' = f_2, f'' = f_3, \theta = f_4, \theta' = f_5, \phi = f_6, \phi' = f_7, \text{Hence, the system of equations becomes } f'_1 = f_2, \tag{18}$$

$$f'_2 = f_3, \tag{19}$$

$$f'_3 = \left(\frac{a_1(1+2\gamma\eta)}{a_2}\right)^{-1} \left[f_2^2 - f_1 f_3 - \left(\frac{2a_1\gamma}{a_2}\right) f_3 + \frac{1}{a_2} (a_3 M + a_1 K) f_2 - \frac{a_7 f_4}{a_2} \right], \tag{20}$$

$$f'_4 = f_5, \tag{21}$$

$$\left(\frac{(a_5+Ra)(1+2\gamma\eta)}{a_6 Pr}\right) f'_5 = \left\{ \left[(f_4 + \delta_1) f_2 - f_1 f_5 - \frac{(a_5+Ra)2\gamma f_5}{a_6 Pr} - \frac{Q f_4}{a_6} - \frac{a_1 Ec(1+2\gamma\eta) f_3^2}{a_6} - \frac{a_3 M Ec f_2^2}{a_6} - a_7 Du(2\gamma f_7 + (1+2\gamma\eta) f_7') \right] \right\} \tag{22}$$

$$f'_6 = f_7, \tag{23}$$

$$f'_7 = \left(\frac{a_7(1+2\gamma\eta)}{Le}\right)^{-1} \left[(f_6 + \delta_2) f_2 - f_1 f_7 - \frac{2a_7\gamma f_7}{Le} - a_7 Sr \{ 2\gamma f_5 + (1+2\gamma\eta) f_5' \} \right] \tag{24}$$

Under the conditions outlined below,

$$f_1(0) = S, f_2(0) = 1, f_4(0) = 1 - \delta_1, f_6(0) = 1 - \delta_2, \text{ as } \eta \rightarrow 0 \tag{25}$$

$$f_2(\infty) = 0, f_4(\infty) = 0, f_6(\infty) = 0 \text{ as } \eta \rightarrow \infty \tag{26}$$

Result and discussion: The effect of magnetic parameter on velocity and temperature is presented in Figures 2a–2c. [Fig.2a] shows that velocity $f'(\eta)$ decreases with increasing M across the boundary layer, accompanied by a reduction in momentum boundary layer thickness. The wall shear stress, proportional to $f''(0)$, also decreases, illustrating that a stronger magnetic field retards fluid flow and suppresses convective momentum transport. In [Fig.2b], increasing M reduces $\theta(\eta)$ at fixed η , thinning the thermal boundary layer. The wall temperature gradient $\theta'(0)$ rises, so the local Nusselt number increases. Hence, in this configuration, a stronger magnetic field enhances wall heat transfer by reducing the thermal layer thickness. A magnetic field induces electric currents in a conducting fluid, generating a Lorentz force that opposes the motion and reduces fluid velocity. This resistive force compresses the velocity boundary layer near the wall. As a result, the coupled thermal boundary layer also thins, enhancing wall heat transfer. [Fig.2c] reveals that magnetic parameter M only slightly reduces $\phi(\eta)$, leading to a modest thinning of the solutal boundary layer. The wall gradient $\phi(0)$ increases slightly, producing a small rise in Sherwood number. The effect is relatively weak under the considered parameter set. Figures 3a–3c analyse the role of curvature parameter γ . [Fig.3a] shows that increasing γ suppresses axial velocity and compresses the momentum boundary layer δ_m . [Fig.3b] indicates that higher curvature enhances heat transfer, producing larger Nusselt numbers, but at the expense of greater wall shear. Conversely, lower curvature (approaching flat plate conditions) yields thicker thermal layers, elevated temperatures away from the wall, and reduced heat-transfer rates. Curvature therefore aids near-wall fluid

cooling. [Fig.3c] demonstrates that higher γ reduces solutal concentration across the boundary layer, thinning the solutal layer and producing steeper gradients $\phi(0)$. Thus, Sherwood number increases with γ , enhancing mass transfer at the wall. The effect of permeability parameter K is depicted in Figures 4a–4c. [Fig.4a] illustrates that increasing K lowers wall shear stress $f''(0)$, reducing momentum transfer. [Fig.4b] indicates that larger K values thin the thermal boundary layer δ_t , enhance the wall gradient $\theta(0)$, and therefore increase Nusselt number. This corresponds to stronger heat extraction at the wall. [Fig.4c] shows that higher K lowers $\phi(\eta)$ across the boundary layer, producing a thinner solutal layer and higher gradient $\phi(0)$, which enhances mass transfer rate at the wall. Figures 5a and 5b highlight the effect of radiation parameter. [Fig.5a] shows that $\theta(\eta)$ decreases as radiation parameter R increases, leading to faster decay of temperature and a thinner thermal boundary layer. This signifies stronger radiative heat loss. [Fig.5b] shows that concentration $\phi(\eta)$ decreases more rapidly with increasing Ra , producing thinner concentration layers. Radiation accelerates solutal diffusion and reduces concentration levels within the boundary layer. Figures 6a and 6b explore the effect of Prandtl number. [Fig.6a] demonstrates that $\theta(\eta)$ decreases more rapidly with Pr , giving a thinner thermal layer. High Pr fluids have low thermal diffusivity, confining heat near the wall. [Fig.6b] indicates that concentration $\phi(\eta)$ decays more slowly as Pr rises, leading to a thicker solutal boundary layer. Thus, higher Pr enhances solutal retention in the boundary layer. The role of heat source parameter Q is presented in Figures 7a and 7b. [Fig.7a] shows that increasing Q raises $\theta(\eta)$, thickening the thermal boundary layer and retaining higher temperatures. [Fig.7b] reveals that larger Q reduces $\phi(\eta)$, since additional thermal energy promotes diffusion and reduces species concentration near the surface. The Eckert number effect is given in Figures 8a and 8b. [Fig.8a] shows that higher Ec raises $\theta(\eta)$ because viscous dissipation converts kinetic energy into heat, thickening the thermal boundary layer. [Fig.8b] shows that increasing Ec lowers $\phi(\eta)$, as viscous heating promotes solutal diffusion and reduces concentration. Thermal buoyancy effects are highlighted in Figures 9a–9c. [Fig.9a] shows that velocity $f'(\eta)$ increases with λ , thickening the momentum boundary layer. [Fig.9b] indicates that $\theta(\eta)$ decreases with λ , because stronger buoyancy enhances convection, removing heat quickly. [Fig.9c] shows that concentration $\phi(\eta)$ decreases with λ due to accelerated mass transfer away from the surface. Figures 10a–10c describe the Dufour effect. [Fig.10a] shows that velocity $f'(\eta)$ increases with Du , thickening the momentum layer. [Fig.10b] shows that $\theta(\eta)$ rises with Du , thickening the thermal layer. [Fig.10c] indicates that

concentration $\phi(\eta)$ increases with Du , thickening the solutal boundary layer. The Dufour effect enhances both heat and mass retention within the boundary layer. The Lewis number effect is shown in Figures 11b and 11c. [Fig.11b] demonstrates that higher Le decreases $\theta(\eta)$, thinning the thermal boundary layer. [Fig.11c] shows that higher Le increases $\phi(\eta)$, thickening the solutal layer. Thus, higher Le favors mass retention over heat diffusion. Figures 12a and 12b present the Soret effect. [Fig.12a] shows that $\theta(\eta)$ increases with Sr , thickening the thermal boundary layer. [Fig.12b] indicates that concentration $\phi(\eta)$ increases with Sr , thickening the solutal boundary layer. Thermal diffusion thus enhances both heat and mass transport. Figures 13a–13c display the impact of stratification δ_1 . [Fig.13a] shows that higher δ_1 increases velocity, thickening the momentum layer. [Fig.13b] shows that $\theta(\eta)$ increases slightly with δ_1 , while [Fig.13c] shows that $\phi(\eta)$ increases with δ_1 , indicating stronger stratification retains both heat and mass near the wall. Figures 14a–14c examine the effect of δ_2 . [Fig.14a] shows that velocity decreases with δ_2 , thinning the momentum layer. [Fig.14b] indicates that $\theta(\eta)$ decreases with δ_2 , thinning the thermal layer. [Fig.14c] shows that $\phi(\eta)$ decreases with δ_2 , reducing solutal transport. Thus, δ_2 suppresses both heat and mass fields. Figures 15b and 15c describe δ_3 effects. [Fig.15b] shows that $\theta(\eta)$ increases with δ_3 , strengthening the thermal boundary layer. [Fig.15c] indicates that $\phi(\eta)$ decreases with δ_3 , reducing solutal concentration near the wall. The role of nanoparticle volume fractions is shown in Figures 16–18. [Fig.16] shows that increasing Cu volume fraction ϕ_1 decreases $\theta(\eta)$, improving heat transfer. [Fig.17] shows that increasing Al_2O_3 fraction ϕ_2 decreases $\theta(\eta)$, also improving thermal conductivity. [Fig.18] shows that increasing TiO_2 fraction ϕ_3 decreases $\theta(\eta)$, confirming its effectiveness in enhancing cooling performance.

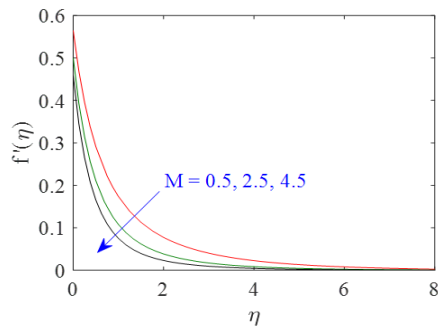


Fig. 2(a). Velocity profiles for distinct M

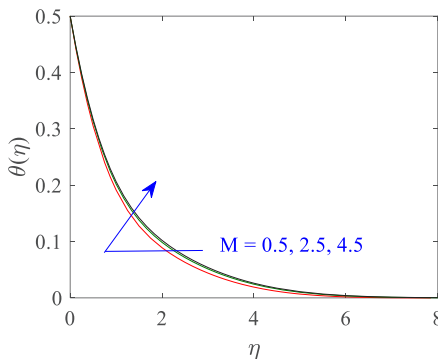


Fig. 2(b). Temperature profiles for distinct M

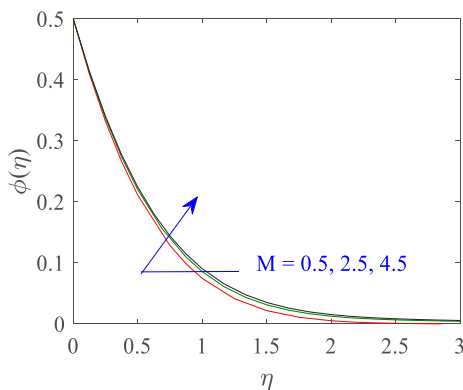


Fig. 2(c). Concentration profiles for distinct M

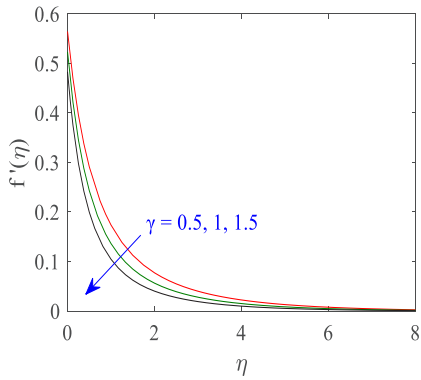


Fig. 3(a). Velocity profiles for distinct γ

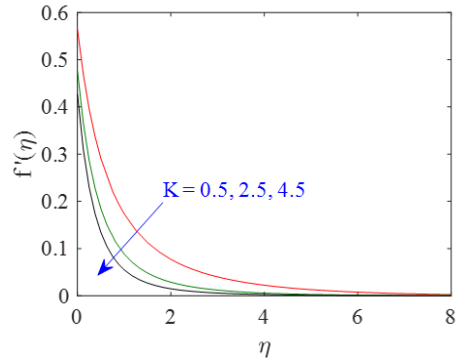


Fig. 4(a). Velocity profiles distinct K

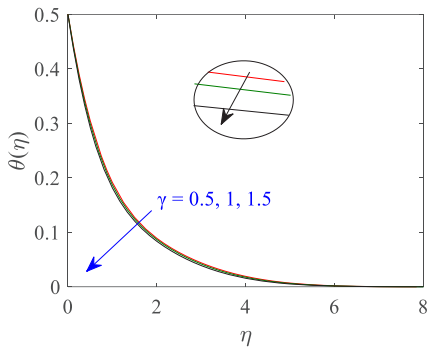


Fig. 3(b). Temperature profiles for distinct γ

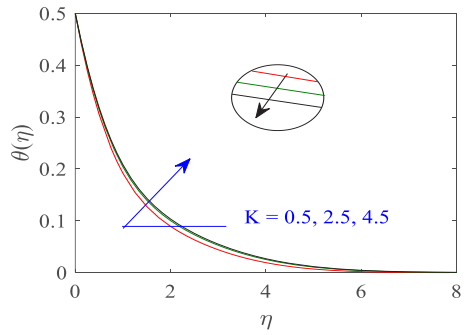


Fig. 4(b). Temperature profiles for distinct K

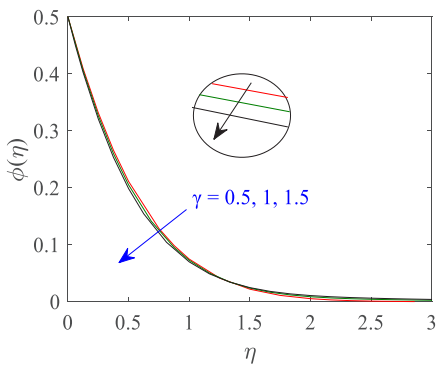


Fig. 3(c). Concentration profiles for distinct γ

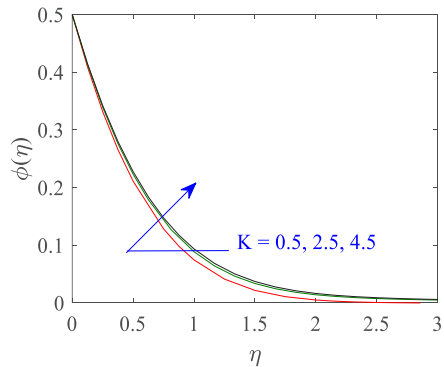


Fig. 4(c). Concentration profiles for distinct K

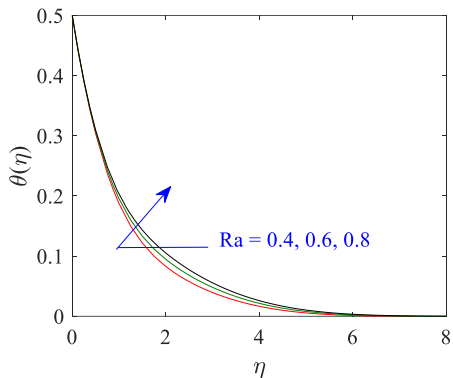


Fig. 5(a). Temperature profiles for distinct Ra

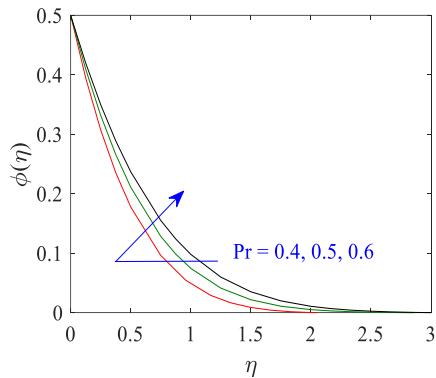


Fig. 6(b). Concentration profiles for distinct Pr

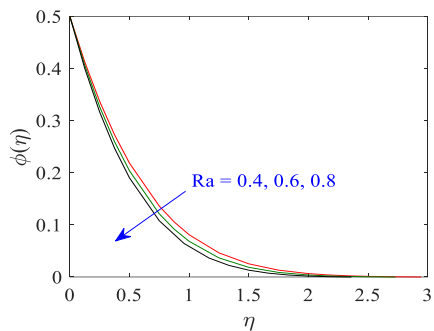


Fig. 5(b). Concentration profiles for distinct Ra

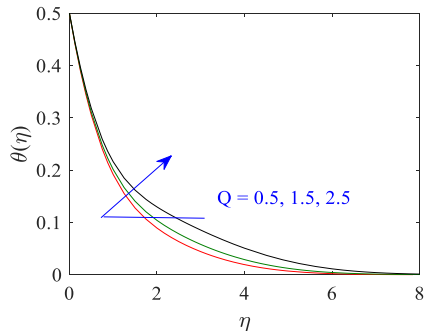


Fig.7(a). Temperature profiles for distinct Q

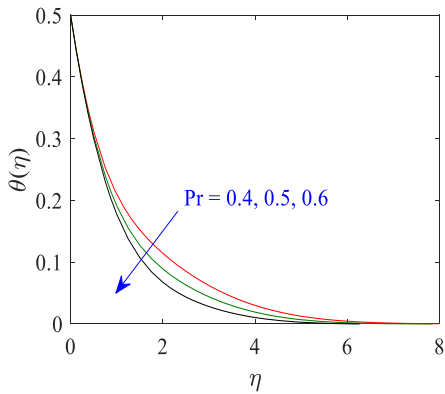


Fig. 6(a). Temperature profiles for distinct Pr

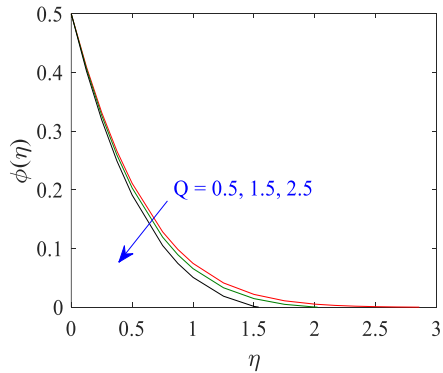


Fig. 7(b). Concentration profiles for distinct Q

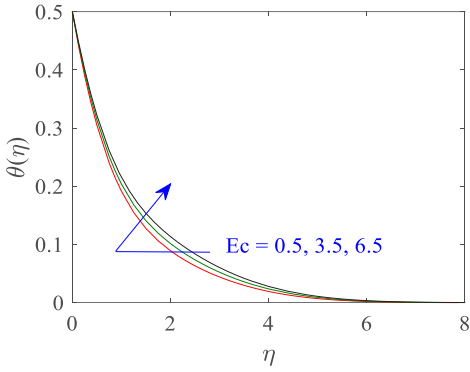


Fig. 8(a). Temperature profiles for distinct Ec

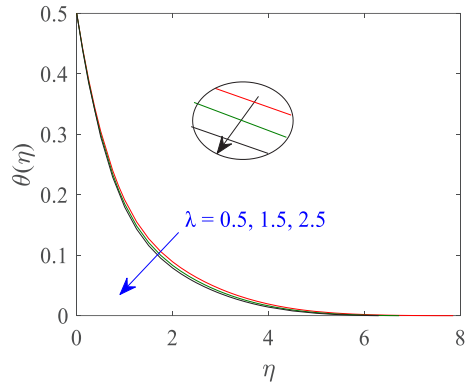


Fig. 9(b). Temperature profiles for distinct λ

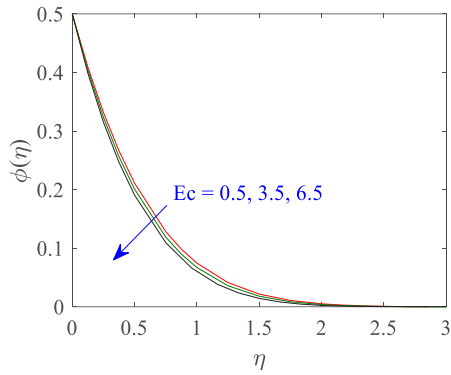


Fig. 8(b). Concentration profiles for distinct Ec

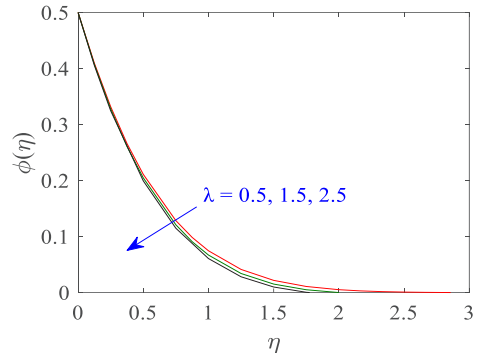


Fig. 9(c). Concentration profiles for distinct λ

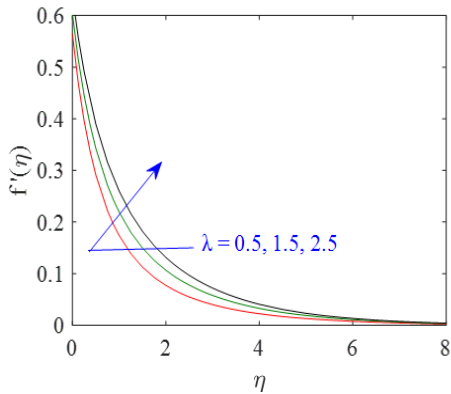


Fig. 9(a). Velocity profiles distinct λ

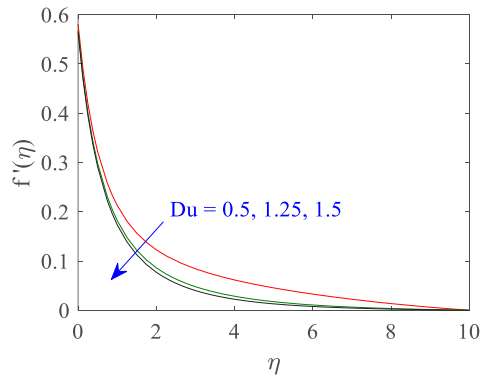


Fig. 10(a). Velocity profiles distinct Du

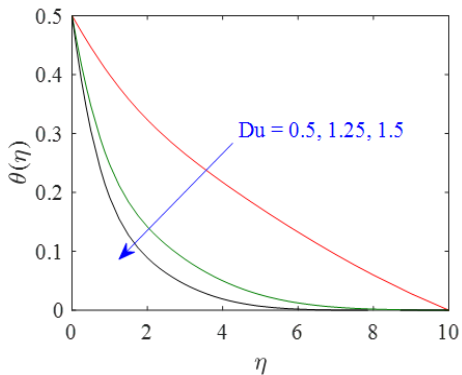


Fig. 10(b). Temperature profiles for distinct Du

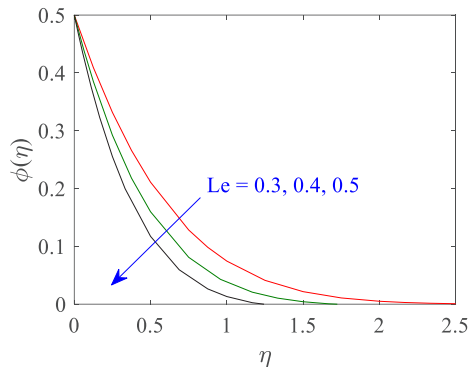


Fig. 11(b). Concentration profiles for distinct Le

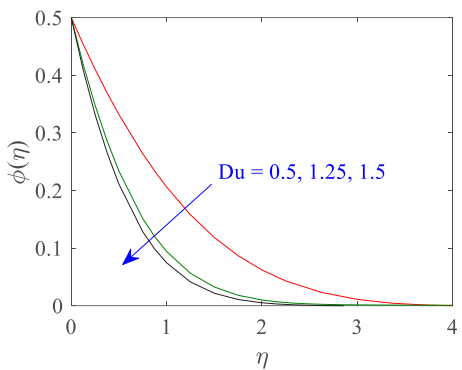


Fig. 10(c). Concentration profiles for distinct Du

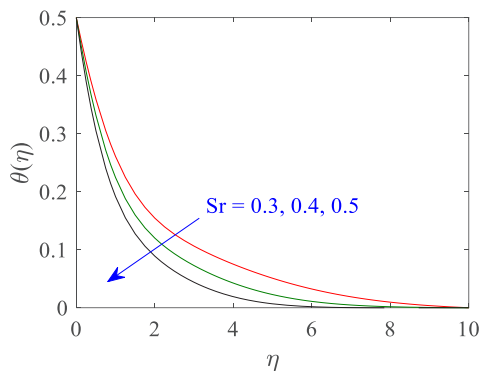


Fig. 12(a). Temperature profiles for distinct Sr

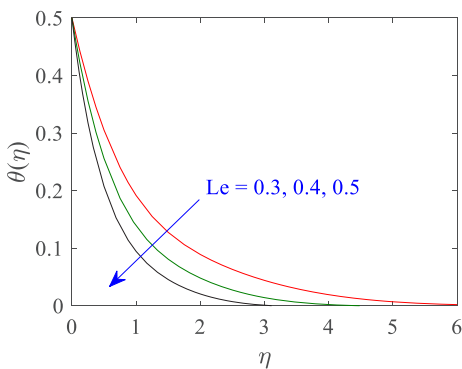


Fig. 11(a). Temperature profiles for distinct Le

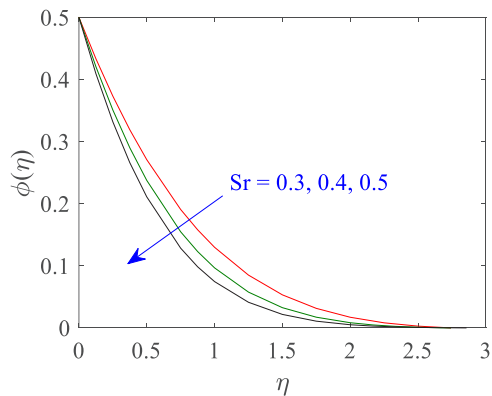


Fig. 12(b). Concentration profiles for distinct Sr

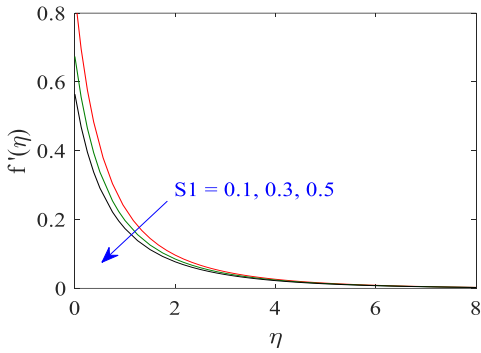


Fig. 13(a). Velocity profiles for distinct S1

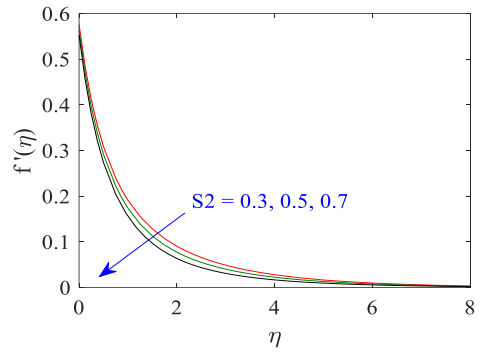


Fig. 14(a) Velocity profiles for distinct S2

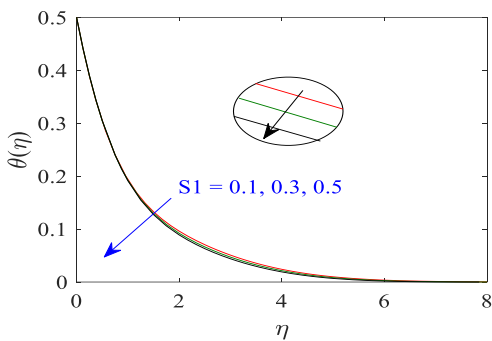


Fig. 13(b). Temperature profiles for distinct S1

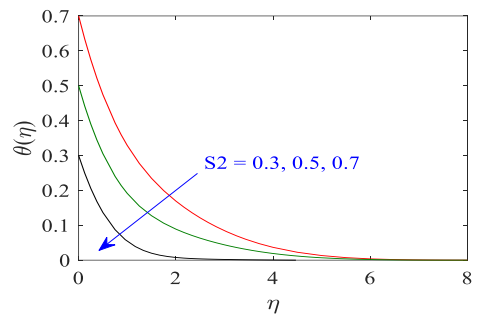


Fig. 14(b). Temperature profiles for distinct S2

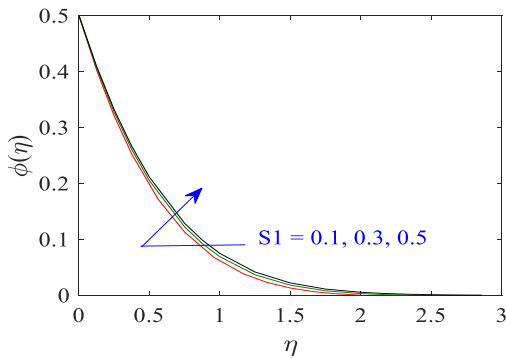


Fig. 13(c). Concentration profiles for distinct S1

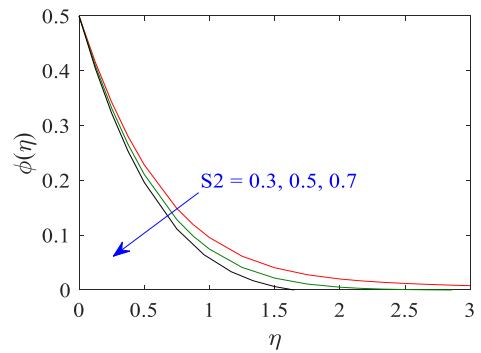


Fig. 14(c). Concentration profiles for distinct S2

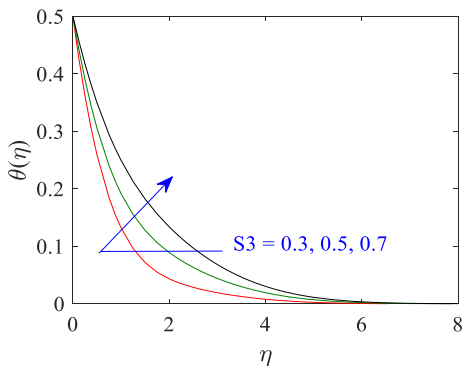


Fig. 15(a). Temperature profiles for distinct S3

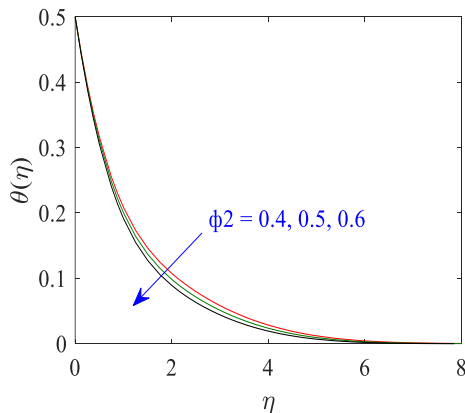


Fig. 17. Temperature profiles for distinct ϕ_2 .

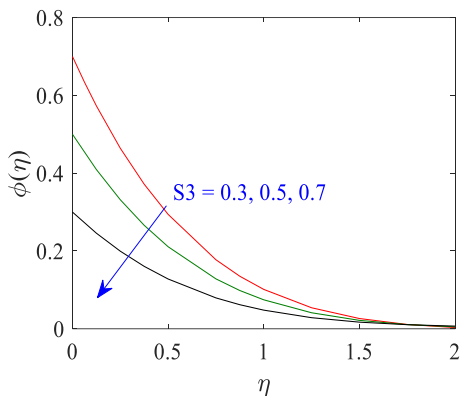


Fig. 15(b). Concentration profiles for distinct S3.

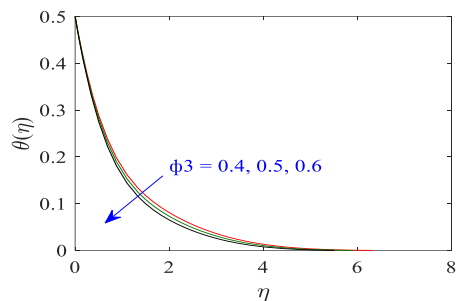


Fig. 18. Temperature profiles for distinct ϕ_3 .

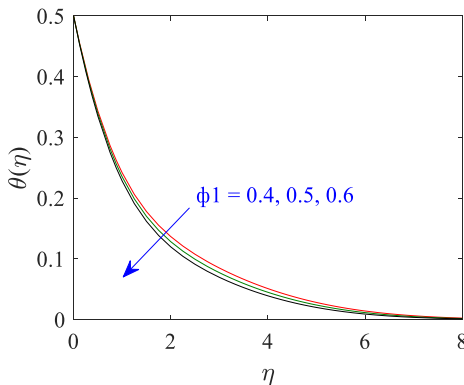


Fig. 16. Temperature profiles for distinct ϕ_1 .

Parameter	$C_f (Re)^{-\frac{1}{2}}$	$Nu(Re)^{\frac{1}{2}}$	$Sh(Re)^{\frac{1}{2}}$
$\zeta = 0.4$	-1.25515	1.58144	1.54950
$\zeta = 0.5$	-1.27962	1.95676	1.81886
$\zeta = 0.6$	-1.30235	2.40044	2.09404
$M = 0.5$	-1.27962	1.95676	1.81886
$M = 2.5$	-1.47026	1.85297	1.75954
$M = 4.5$	-1.59191	1.80465	1.72960
$K = 0.5$	-1.27962	1.95676	1.81886
$K = 2.5$	-1.53851	1.83611	1.73425
$K = 4.5$	-1.68292	1.79021	1.70036

$Ra = 0.4$	-1.28049	1.86046	1.75172
$Ra = 0.6$	-1.27878	2.05296	1.88524
$Ra = 0.8$	-1.27721	2.24487	2.01596
$Pr = 0.4$	-1.27581	1.94426	2.14057
$Pr = 0.5$	-1.27962	1.95676	1.81886
$Pr = 0.6$	-1.28265	1.96770	1.59435
$Q = 0.5$	-1.27962	1.95676	1.81886
$Q = 1.5$	-1.27719	1.90233	1.87933
$Q = 2.5$	-1.27289	1.83373	1.96640
$Ec = 0.5$	-1.27962	1.95676	1.81886
$Ec = 3.5$	-1.27714	1.80458	1.94081
$Ec = 6.5$	-1.27483	1.69374	2.06238
$Du = 0.5$	-1.23087	0.44439	0.88676
$Du = 1.25$	-1.26813	1.44952	1.61193
$Du = 1.5$	-1.27962	1.95676	1.81886
$Le = 0.3$	-1.27962	1.95676	1.81886
$Le = 0.4$	-1.29018	2.74440	2.36073
$Le = 0.5$	-1.29884	3.84900	2.91694
$Sr = 0.3$	-1.26404	1.28768	1.30385
$Sr = 0.4$	-1.27237	1.61397	1.57362
$Sr = 0.5$	-1.27962	1.95676	1.81886
$\lambda = 0.5$	-1.27962	1.95676	1.81886
$\lambda = 1.5$	-1.16674	2.01983	1.86184
$\lambda = 2.5$	-1.06108	2.07388	1.89864
$\gamma = 0.5$	-1.27962	1.95676	1.81886
$\gamma = 1$	-1.40074	2.06426	1.89574
$\gamma = 1.5$	-1.51886	2.19166	1.97840
$S_1 = 0.1$	-2.14382	1.09751	1.96744

$S_1 = 0.3$	-1.59625	1.40509	1.87699
$S_1 = 0.5$	-1.27962	1.95676	1.81886
$S_2 = 0.3$	-1.24561	2.19764	1.20825
$S_2 = 0.5$	-1.27962	1.95676	1.81886
$S_2 = 0.7$	-1.31422	1.70751	3.21418
$S_3 = 0.3$	-1.29017	2.53036	2.54426
$S_3 = 0.5$	-1.27962	1.95676	1.81886
$S_3 = 0.7$	-1.26951	1.43396	1.09131
$\phi_1 = 0.4$	-1.25515	1.58144	1.54950
$\phi_1 = 0.5$	-1.18566	1.48076	1.53242
$\phi_1 = 0.6$	-1.11984	1.38817	1.51839
$\phi_2 = 0.4$	-1.13267	1.39304	1.52144
$\phi_2 = 0.5$	-1.19209	1.48342	1.53406
$\phi_2 = 0.6$	-1.25515	1.58144	1.54950
$\phi_3 = 0.4$	-1.17998	2.04194	2.01628
$\phi_3 = 0.5$	-1.23929	2.21130	2.05322
$\phi_3 = 0.6$	-1.30235	2.40044	2.09404

Conclusion:

- The speed distribution exhibits a declining trend as the magnetic parameter M , permeability parameter K , prandlt number Pr , Dufour parameter Du , Soret parameter Sr , thermal stratification parameter S_1 , and suction parameter S are raised. Conversely, it exhibits an increasing tendency with high quantities of the curvature parameter γ and the thermal generation parameter Q , radiation parameter Ra , Eckert number Ec , and heat buoyancy parameter λ .
- The thermal distribution shows a decrease in trend when the following measurements are measured: Heat generation parameter Q , thermal radiation parameter Ra , heat buoyancy parameter λ , heat stratification parameter S_1 , concentration stratification parameter S_1 , curvature parameter γ , and Eckert number Ec . Lewis parameter Le , Dufour parameter Du , and Soret parameter Sr . The $CuO - MgO - TiO_2$ concentration parameters ϕ_1 , ϕ_2 , and ϕ_3 of Sr and nanoparticles rise with the magnetic

parameter. M , prandtl number Pr , and permeability parameter K .

- The concentration profile shows a declining trend as the concentration stratification parameter S_2 , the Levis parameter Le , the Dufour parameter Du , the temperature buoyancy parameter λ , and the curvature parameter γ rise. On the other hand, it shows an increase as the magnetic parameter M , permeability parameter K , thermal stratification parameter S_1 , and prandtl number Pr increase.
- Radiation parameter Ra and thermal buoyancy parameter λ increase the rates of skin fraction, heat transfer, and Sherwood number; permeability parameter K and magnetic parameter M have the opposite effect.
- For heat generation parameters Q and Ec , skin friction and Sherwood number increase; yet, for thermal stratification factors S_1 and Pr , opposite behavior is seen.
- Curvature parameter γ , Dufour parameter Du , Levis parameter Le , Soret parameter Sr , and nanoparticle the $Cuo-Mgo-TiO_2$ concentration parameter ϕ_2, ϕ_3 are the parameters that lead to increases in Nusselt and Sherwood numbers. Yet the $Cuo-Mgo-TiO_2$ concentration parameter ϕ_1 has the opposite effect.
- The concentration stratification parameter S_2 reduces rates of skin friction and heat transfer.

References:

1. H. Xie., W. Yu, W. Chen MgO nanofluids, higher thermal conductivity and lower viscosity among ethylene glycol-based nanofluids containing oxide nanoparticles. *J. Exp. Nanosci.* 5(5), 463-472, (2010)
2. S. Suresh, K. P. Venkataraj, P. Selvakumar, M. Chandrasekar, Synthesis of Al_2O_3-Cu /water hybrid nanofluids using two step method and its thermo physical properties. *Colloids and Surfaces A: Physicochem. Eng. Asp.* 388(1-3), 41-48, (2011)
3. M. K. A. Mohamed, N. M. Sarif, N. A. Z. M. Noar, M. Z. Salleh, A. M. Ishak, Mixed convection boundary layer flow on a horizontal circular cylinder in a nanofluid with viscous dissipation effect. *Malays. J. Fundam. Appl. Sci.* 14(1), 32-39, (2018)
4. A. J. Chamkha, A. S. Dogonchi, D. D. Ganji, Magneto-hydrodynamic flow and heat transfer of a hybrid nanofluid in a rotating system among two surfaces in the presence of thermal radiation and Joule heating. *AIP Adv.* 9(2), (2019)
5. M. M. Maskeen, A. Zeeshan, O. U. Mehmood, M. Hassan, Heat transfer enhancement in hydromagnetic alumina-copper/water hybrid nanofluid flow over a stretching cylinder. *J. Therm. Anal. Calorim.* 138, 1127-1136, (2019)
6. A. Ali, F. Iqbal, D. N. Khan Marwat, S. Asghar, M. Awais, Soret and Dufour effects between two rectangular plane walls with heat source/sink. *Heat Transf. Asian Res.* 49(1), 614-625, (2020).
7. E. Aminian, H. Moghadasi, H. Saffar, Magnetic field effects on forced convection flow of a hybrid nanofluid in a cylinder filled with porous media : A numerical study. *J. Therm. Anal. Calorim.* 141, 2019-2031, (2020)
8. E. R. El-Zahar, A. M. Rashad, W. Saad, L. F. Seddek, Magneto-hybrid nanofluids flow via mixed convection past a radiative circular cylinder. *Sci. Rep.* 10(1), 10494, (2020)
9. I. Filahi, M. Bourich, M. Hasnaoui, A. Amahmid, Analytical and Numerical Study of Soret and Dufour Effects on Thermosolutal Convection in a Horizontal Brinkman Porous Layer with a Stress-Free Upper Boundary. *Math. Probl. Eng.* 2020(1), 4046570, (2020)
10. N. S. Khashi, N. M. Arifin, I. Pop, N. S. Wahid, Flow and heat transfer of hybrid nanofluid over a permeable shrinking cylinder with Joule heating: A comparative analysis. *Alex. Eng. J.* 59(3), 1787-1798, (2020)
11. B. Kristiawan, A. I. Rifai, K. Enoki, A. T. Wijayanta, T. Miyazaki, Enhancing the thermal performance of TiO_2 /water nanofluids flowing in a helical microfin tube. *Powder Technol.* 376, 254-262, (2020)
12. C. K. Kumar, S. Srinivas, & A. S. Reddy, MHD pulsating flow of Casson nanofluid in a vertical porous space with thermal radiation and Joule heating. *J. Mech.* 36(4), 535-549 (2020).
13. M. Ma, Y. Zhai, P. Yao, Y. Li, & H.Wang, Synergistic mechanism of thermal conductivity enhancement and economic analysis of hybrid nanofluids. *Powder Technol.* 373, 702-715 (2020).
14. J. A. Okello, W. N. Mutuku, A. O. Oyem, Analysis of ethylene glycol (EG)-based ((Cu- Al_2O_3), (Cu- TiO_2), ($TiO_2-Al_2O_3$)) hybrid nanofluids for optimal car radiator coolant. *J. Eng. Res. Rep.* 17(2), 34-50, (2020).
15. N. C. Roy, L. K. Saha, M. Sheikholeslami, Heat transfer of a hybrid nanofluid past a circular cylinder in the presence of thermal radiation and viscous dissipation. *AIP Adv.* 10(9), (2020)
16. S. Shafie, R. Mahat, F. Januddi, Numerical Solutions of Mixed Convection Flow Past a Horizontal Circular Cylinder with Viscous Dissipation in Viscoelastic Nanofluid. *J. Adv. Res. Micro Nano Eng.* 1(1), 24-37, (2020)
17. Z. Zhou, Z. Wang, & M. Yang, Double diffusive natural convection in open cavity under the Soret and Dufour effects. *Front. Heat Mass Transf.* 14, (2020).
18. O. P. Meena, P. Janapatla, A. J. Chamkha, Influence of Soret and Dufour effects on mixed convection flow over a vertical cone with injection/suction effects. *Journal of Porous Media, J. Porous Media.* 24(4), (2021)
19. I. H. Qureshi, M. Nawaz, M. A. Abdel-Sattar, S. Aly, M. Awais, Numerical study of heat and

- mass transfer in MHD flow of nanofluid in a porous medium with Soret and Dufour effects. *Heat Transf.* 50(5), 4501-4515, (2021).
20. M. G. Reddy, P. Vijayakumari, K. G. Kumar, S. A. Shehzad, Zero-mass flux and Cattaneo–Christov heat flux through a Prandtl non-Newtonian nanofluid in Darcy–Forchheimer porous space. *Heat Transf.* 50(1), 220-233, (2021)
 21. B. Venkateswarlu, P. V. Satyanarayana, Cu-Al₂O₃/H₂O hybrid nanofluid flow past a porous stretching sheet due to temperature-dependent viscosity and viscous dissipation. *Heat Transf.* 50(1), 432-449, (2021)
 22. P. Yesodha, M. Bhuvaneshwari, S. Sivasankaran, K. Saravanan, Convective heat and mass transfer of chemically reacting fluids with activation energy along with Soret and Dufour effects. *Mater. Today Proc.* 42, 600-606, (2021)
 23. N. S. M. Hanafi, W. A. W. Ghopa, R. Zulkifli, S. Abdullah, Z. Harun, M. R. A. Mansor, Numerical simulation on the effectiveness of hybrid nanofluid in jet impingement cooling application. *Energy Rep.* 8, 764-775, (2022)
 24. A. Raza, S. U. Khan, K. Al-Khaled, M. I. Khan, A. U. Haq, F. Alotaibi, S. Qayyum, A fractional model for the kerosene oil and water-based Casson nanofluid with inclined magnetic force. *Chem. Phys. Lett.* 787, 139277, (2022)
 25. Z. Asghar, R. S. Saif, A. Z. Ghaffari, Numerical study of boundary stresses on Jeffery–Hamel flow subject to Soret/Dufour effects. *Proc. Inst. Mech. Eng., Part C: J. Mech. Eng. Sci.* 1088-1105, (2023)
 26. M. V. Chepak-Gizbrekht, A. G. Knyazeva, the influence of Soret and Dufour cross-effects on laser surface treatment of metal accompanied by solid-phase chemical reaction. *Olid. State. Ionics.* 400, 116323, (2023).
 27. J. S. Huang, Chemical reaction and activation energy on heat and mass transfer for convective flow along an inclined surface in Darcy porous medium with Soret and Dufour effects. *J. Mech.* 39, 88-104, (2023)
 28. M. Imran, M. Naveed, Z. Abbas, Dynamics of Soret and Dufour effects on oscillatory flow of couple stress fluid due to stretchable curved surface. *Adv. Mech. Eng.* 15(2), 16878132231156742, (2023)
 29. S. Li, M. I. Khan, M. Rafiq, S. A. B. Abdelmohsen, S. S. Abdullaev, M. S. Amjad, Optimized framework for Darcy–Forchheimer flow with chemical reaction in the presence of Soret and Dufour effects: a shooting technique. *Chem. Phys. Lett.* 825, 140578, (2023)
 30. N. K. Mishra, M. Sharma, B. K. Sharma, U. Khanduri, Soret and Dufour effects on MHD nanofluid flow of blood through a stenosed artery with variable viscosity. *Int. J. Mod. Phys. B.* 37(30), 2350266, (2023).
 31. P. M. Patil, B. Goudar, M. A. Sheremet, Tangent hyperbolic ternary hybrid nanofluid flow over a rough-yawed cylinder due to impulsive motion. *J. Taibah Univ. Sci.* 17(1), 2199664, (2023)
 32. S. Rehman, S. B. H. Hassine, E. Tag Eldin, S. O. Shah, Investigation of entropy production with thermal analysis under Soret and Dufour effects in MHD flow between convergent and divergent channels. *ACS omega.* 8(10), 9121-9136, (2023)
 33. A. Shafiq, A. B. Çolak, T. N. Sindhu, Analyzing activation energy and binary chemical reaction effects with artificial intelligence approach in axisymmetric flow of third grade nanofluid subject to Soret and Dufour effects. *Heat Transf. Res.* 54(3), (2023)
 34. M. Yasir, M. Khan, A. S. Alqahtani, M. Y. Malik, Numerical study of axisymmetric hybrid nanofluid MgO–Ag/H₂O flow with non-uniform heat source/sink. *Alex. Eng. J.* 75, 439-446, (2023)
 35. U. Farooq, T. Liu, U. Farooq, S. Majeed, Non-similar analysis of bioconvection MHD micropolar nanofluid on a stretching sheet with the influences of Soret and Dufour effects. *Appl. Water Sci.* 14(6), 116 (2024)
 36. R. S. Nath, R. K. Deka, A numerical study on the mhd ternary hybrid nanofluid (cu-al₂o₃-tio₂/h₂o) in presence of thermal stratification and radiation across a vertically stretching cylinder in a porous medium. *East Eur. J. Phys.* (1), 232-242, (2024)
 37. S. Naz, T. Hayat, M. A. Sadiq, S. Momani, Significance of nonlinear radiation in entropy generated flow of ternary-hybrid nanofluids with variable thermal conductivity and viscous dissipation. *Ain Shams Eng. J.* 15(7), 102792, (2024)
 38. K. Sudarmozhi, D. Iranian, I. Khan, F. Hajje, A. S. Omer, F. A. Altayyar, Heat generation in dual convection Non-Newtonian MHD Darcy's flow with Soret and Dufour effects *Case Stud. Therm. Eng.* 53, 103704, (2024)
 39. Z. Ullah, M. A. Said, M. D. Alsulami, S. Al Armi, N. H. Eljaneid, A. Hakami, N. B. Khedher, Thermal radiation and soret/dufour effects on amplitude and oscillating frequency of darcian mixed convective heat and mass rate of nanofluid along porous plate. *Case Stud. Therm. Eng.* 59, 104562, (2024)
 40. B. Venkateswarlu, P. V. S. Narayana, S. W. Joo, Exploration of entropy analysis and viscous dissipation on radially convective flow of (Cu-Al₂O₃: h₂O) hybrid nanofluid over a stretching disk. *Asia-Pac. J. Chem. Eng.* 19(1), e3002, (2024)